Journal of
Applied
Crystallography
ISSN 0021-8898

Received 30 June 2009
Accepted 10 February 2010

© 2010 International Union of Crystallography
Printed in Singapore – all rights reserved

Structure of $PbTe(SiO_2)/SiO_2$ multilayers deposited on Si(111)

Guinther Kellermann,[a]* Eugenio Rodriguez,[b] Ernesto Jimenez,[b] Carlos Lenz Cesar,[b] Luiz Carlos Barbosa[b] and Aldo Felix Craievich[c]

[a]Laboratório Nacional de Luz Síncrotron, Campinas SP, Brazil, [b]DEQ, Instituto de Física Gleb Wataghin, Universidade Estadual de Campinas, Campinas SP, Brazil, and [c]Instituto de Física, Universidade de São Paulo, São Paulo SP, Brazil. Correspondence e-mail: keller@lnls.br

The structure of thin films composed of a multilayer of PbTe nanocrystals embedded in SiO_2, named as $PbTe(SiO_2)$, between homogeneous layers of amorphous SiO_2 deposited on a single-crystal Si(111) substrate was studied by grazing-incidence small-angle X-ray scattering (GISAXS) as a function of PbTe content. $PbTe(SiO_2)/SiO_2$ multilayers were produced by alternately applying plasma-enhanced chemical vapour deposition and pulsed laser deposition techniques. From the analysis of the experimental GISAXS patterns, the average radius and radius dispersion of PbTe nanocrystals were determined. With increasing deposition dose the size of the PbTe nanocrystals progressively increases while their number density decreases. Analysis of the GISAXS intensity profiles along the normal to the sample surface allowed the determination of the period parameter of the layers and a structure parameter that characterizes the disorder in the distances between PbTe layers.

1. Introduction

A number of glasses containing semiconductor nanocrystals exhibit highly nonlinear optical properties and fast response times (Tsunetomo *et al.*, 1995; Gleiter, 1989), making them good candidates for applications to telecommunication devices (Reynoso *et al.*, 1995). In these nanocomposites the electron and the hole Bohr radii are larger than the semiconductor nanocrystal size, thus generating strong electron–hole quantum confinement and, as a consequence, an increase in the energy gap between the valence and the conduction electron bands. A simple theoretical model derived by Efros & Efros (1982) demonstrates that the electron energy gap for spherical nanocrystals is proportional to the inverse of the square of their radius. More generally, it was established that the optical properties of this type of nanostructured material strongly depend on the size and shape, and also on the spatial ordering, of the semiconductor nanocrystals. For this reason, a number of scientists are currently trying to develop new processes leading to nanostructured materials containing nanocrystals with controlled shape, average size, size dispersion and spatial correlation (Craievich *et al.*, 2002). The final goal of these investigations is to obtain new nanocomposites with properties tailored for relevant practical applications.

Several techniques, such as transmission electron microscopy (TEM), optical absorption, atomic force microscopy, X-ray diffraction (XRD) and small-angle X-ray scattering (SAXS), have been applied to establish the structure of composites consisting of semiconductor nanoparticles embedded in dielectric matrices. The SAXS technique at grazing incidence (GISAXS) has been used to characterize metallic (d'Acapito *et al.*, 2004; Cohen & Chung, 1991) and semiconductor (Desnica *et al.*, 2004; Buljan *et al.*, 2003) nanoparticles embedded in thin films deposited on the surfaces of flat substrates. By appropriate choices of the grazing-incidence angle and photon energy of the primary X-ray beam, this technique can probe selected slices close to the external surface of the sample, with small thicknesses (typically from 5 nm up to a few hundreds of nanometres). As a consequence, the background of the X-ray scattered photons coming from the substrate bulk volume is minimized. In contrast to TEM experiments, for which the structural information regarding nanocrystal shapes and sizes usually corresponds to a few hundreds of nanoparticles, the GISAXS technique provides similar information but corresponding to a number of particles many orders of magnitude higher ($\sim10^5$–10^{12} particles) distributed over a large area of about 10 mm^2 or more. This allows for a better sampling over a large sample surface.

Herein we report a GISAXS study of the structure of $PbTe(SiO_2)/SiO_2$ multilayers deposited on an Si(111) single-crystal substrate as a function of PbTe content. The number of laser light pulses hitting the PbTe target along the deposition of each PbTe layer is different for every sample studied but the total number of $PbTe/SiO_2$ periods was kept the same for all of them. The GISAXS technique was applied in order to determine the average size, size dispersion and number density of PbTe nanocrystals as well as their dependence on the amount of deposited PbTe, this amount being considered as proportional to the number of laser pulses applied during the

preparation of each PbTe layer. Additionally, the period or average distances between PbTe layers and their fluctuations were determined.

2. Experimental

$PbTe(SiO_2)/SiO_2$ multilayers were grown on a single-crystal Si(111) substrate using a specially designed ultra-high-vacuum chamber (Rodriguez *et al.*, 2006). The glassy SiO_2 layers were obtained by plasma-enhanced chemical vapour deposition (PECVD) using tetramethylorthosilicate (TMOS) as a precursor material. In this procedure the TMOS molecule is cracked by the action of an oscillatory electrical field provided by a 13.56 MHz radiofrequency (RF) source. The $PbTe(SiO_2)$ layers were built up by pulsed laser deposition (PLD) using the second harmonic of an Nd:YAG laser operating in the *Q*-switch regime. The chamber was kept under argon (1.8×10^{-1} mbar; 1 mbar = 0.1 kPa) and TMOS (2.0×10^{-2} bar) atmosphere during the growth of both PbTe nanocrystals and SiO_2 layers.

The thickness of each homogeneous SiO_2 layer is proportional to the time period, t_{RF}, during which the RF is switched on, while the amount of PbTe in each $PbTe(SiO_2)/SiO_2$ layer is proportional to the total number of laser pulses hitting the target during each layer formation. The t_{RF} time periods and the thicknesses of the SiO_2 layers were kept the same for all layers and all samples studied. Each sample was composed of 20 identical $PbTe(SiO_2)/SiO_2$ bi-layers. An additional top layer of SiO_2 was deposited in order to avoid oxidation of the last PbTe layer.

In order to determine the size and size distribution of the PbTe nanocrystals as a function of total PbTe content, several multilayered samples were prepared. All $PbTe(SiO_2)/SiO_2$ multilayers were grown by alternately applying PECVD and PLD techniques, maintaining, for all of them, the same preparation parameters except the number of laser pulses for each PLD step. The number of laser pulses for deposition of a PbTe layer in each sample was varied from 50 to 200.

GISAXS experiments were performed at the XRD2 X-ray diffraction beamline of the Brazilian Synchrotron Light Laboratory (LNLS) using a 0.15498 nm wavelength beam. The two-dimensional patterns of the GISAXS intensity were recorded following the procedure proposed by Salditt *et al.* (1994), in which the incidence angle of the X-ray beam on the multilayer external surface is kept constant and the two-dimensional scattering intensity is measured using a 10×10 cm imaging plate with a 10^6 dynamical range and a 0.2×0.2 mm pixel size. In order to determine the contribution of the SiO_2 layers to the total scattered intensity, the GISAXS produced by a similar sample prepared under the same conditions but without deposition of PbTe layers was also measured. The results for the sample without PbTe showed a weak and approximately constant scattering intensity except at very small angles for which a slight contribution from the totally reflected beam was noticed. This weak contribution was subtracted from the total intensity produced by the different studied $PbTe(SiO_2)/SiO_2$ multilayers. A four-circle diffractometer was used for the procedure of sample alignment and adjustment of the incidence angle. The angular divergences of the X-ray beam in the vertical and horizontal directions were 0.005 and 0.2°, respectively. Measurements were performed at two different sample-to-detector distances, 354.5 and 868.5 mm, allowing us to achieve $|q|$ values in the 0.15–5 nm^{-1} range. The resolutions in reciprocal space for these configurations, determined by the point spread function of the direct beam on the two-dimensional detector, were δq_z = 0.03 $nm^{-1} \times \delta q_{\|}$ = 0.2 nm^{-1} and δq_z = 0.012 $nm^{-1} \times \delta q_{\|}$ = 0.08 nm^{-1}, respectively.

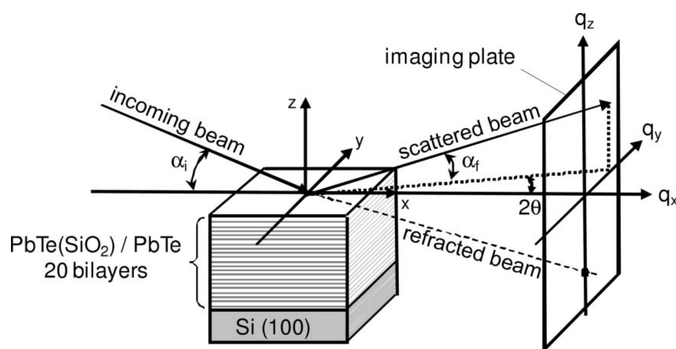

Figure 1
Schematic geometry of the GISAXS experiments.

A schematic representation of the geometry used in our GISAXS experiment is given in Fig. 1. The GISAXS pattern was determined as a function of the photon momentum transfer given by

$$\mathbf{q} = \mathbf{k}_f - \mathbf{k}_i = \begin{pmatrix} q_x \\ q_y \\ q_z \end{pmatrix} = \frac{2\pi}{\lambda} \begin{pmatrix} \cos 2\theta \cos \alpha_f - \cos \alpha_i \\ \sin 2\theta \cos \alpha_f \\ \sin \alpha_i + \sin \alpha_f \end{pmatrix}, \quad (1)$$

where λ is the wavelength of the X-rays, $\mathbf{k}_i$ and $\mathbf{k}_f$ are the wavevectors of the incidence and scattered X-ray photons, α_i and α_f are the angles made by the incidence and scattered X-ray beam, respectively, with the surface of the sample, and 2θ is the angle between the $\mathbf{k}_i$ and $\mathbf{k}_f$ vectors projected onto the multilayer surface (Rauscher *et al.*, 1999).

3. Experimental results and modelling

Previous TEM images of a $PbTe(SiO_2)/SiO_2$ multilayer (Rodriguez *et al.*, 2005) indicated that PbTe layers are not homogeneous but, instead, they consist of a set of closely located and quasi-randomly dispersed PbTe nanocrystals. TEM images also demonstrated that the PbTe nanocrystals have a nearly spherical shape with an average radius in the nanometre range and a rather narrow radius dispersion.

In order to obtain a structural description averaged over a wide multilayer area, the $PbTe(SiO_2)/SiO_2$ samples were studied by the GISAXS technique by adequately selecting the grazing-incidence angle. The irradiated area of each sample was approximately 3×20 mm (footprint of the X-ray beam on the surface of the flat sample).

The real part of the refraction index was determined from the relation $1 - \delta = \cos \alpha_c$ (Tolan, 1999), where α_c is the critical

angle of total external reflection. The multilayer α_c angles, determined from X-ray reflectivity experiments, are close to 0.22°, this being the value expected for the critical angle of total reflection of SiO_2 glass at the given X-ray photon energy (8 keV). Thus the refraction index of silica glass was used in our calculation of the $|T(\alpha_i)|$ and $|T(\alpha_f)|$ Fresnel transmission functions that modulate the scattering curves over a q range close to $\alpha_f = \alpha_c$.

Fig. 2 shows the two-dimensional GISAXS intensity pattern corresponding to a $PbTe(SiO_2)/SiO_2$ multilayer prepared by applying 150 laser pulses, the incidence angle of the X-ray beam being $\alpha_i = 0.3°$. Under this experimental condition the estimated value of the penetration length Λ – the depth for which the intensity falls to $1/e$ of its value at the surface – is equal to 360 and 220 nm for multilayers prepared with 100 and 200 laser pulses, respectively. As will be shown from the values of the multilayer period determined in §4.2 and taking account of the fact that all samples are composed of 20-layer periods, these penetration lengths correspond to about 1 and 2/3 of the total thicknesses of these multilayers, respectively.

The GISAXS intensity pattern corresponding to samples prepared using 150 laser pulses (Fig. 2) exhibits a set of horizontally elongated spots, periodically spaced along the direction normal to the sample surface (z axis), superposed onto an approximately isotropic small-angle X-ray scattering intensity extending over a much wider angular range. Similar features were also observed in the GISAXS patterns corresponding to multilayers prepared with 100 and 200 laser pulses. However, the pattern corresponding to the sample with minimum PbTe content – prepared by applying 50 laser pulses – only exhibits a weak and nearly constant intensity pattern, suggesting that, under this low deposition condition, PbTe clusters are absent or very small so that their effect on the X-ray scattering curves is too weak to be detected.

X-ray scattering profiles displaying periodic maxima along the direction perpendicular to the layers (Fig. 2), also referred to as Bragg sheets (Salditt *et al.*, 1994; Paniago *et al.*, 1997), were previously observed for many other multilayered materials with rough interfaces. For the $PbTe(SiO_2)/SiO_2$ multilayers studied here, where the PbTe layers are composed of a set of individual nanocrystals, the X-ray scattering maxima are attributed to the spatial correlation between the PbTe nanocrystals in different PbTe layers. In this case the horizontally elongated intensity spots that can be observed in Fig. 2 are sections through the maxima of the structure function related to the one-dimensional lattice corresponding to PbTe nanocrystal layers alternated by amorphous SiO_2 layers. The average distance between the maxima along the q_z direction is $\Delta q_z = 2\pi/D$, where D is the multilayer period. The fact that several maxima are observed in the GISAXS patterns indicates that the spatial correlation between PbTe layers extends over a long distance, along the direction normal to the layers.

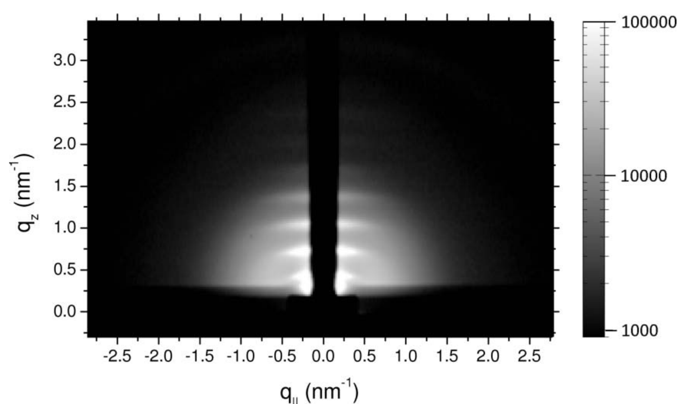

Figure 2
A two-dimensional GISAXS image corresponding to a $PbTe(SiO_2)/SiO_2$ multilayer on Si(111). The number of laser pulses used in the PbTe deposition was 150. The non-irradiated vertical strip in the centre of the image is the shadow of the beam-stopper used to block the transmitted and the specularly reflected X-ray beams.

In general, besides the vertical correlation, lateral correlation between nanocrystals in different layers can also take place if the structural features are replicated from layer to layer. For example, replication of the interface roughness was previously observed in a number of multilayer systems in which all layers have homogeneous composition (Holý *et al.*, 1999). Propagation of spatial order from layer to layer was also observed in multilayers formed by nanoparticles. An example is the vertical alignment of Ge quantum dots by epitaxic grown on Si(100) reported by Kegel *et al.* (1999) for a Ge/Si(100) multilayer. In this case, the alignment is a consequence of the formation of preferred nucleation sites in stress fields induced by the buried dots. In particular deposition conditions, self-arrangement of nanoparticles can also take place in stacking processes of nanoparticle layers separated by amorphous layers, provided the amorphous layers are thin enough to allow for a significant replication of the topological features of the buried nanoparticles (Babonneau *et al.*, 2000).

On the other hand, for the $PbTe(SiO_2)/SiO_2$ multilayered samples studied here, the thickness of the SiO_2 layers between PbTe nanoparticle layers is much larger than the average diameter of the nanocrystals. The expected consequence is that the topography of the surface containing the deposited PbTe nanoparticles is significantly smoothed after the deposition of the SiO_2 layer. In this case the top surfaces of the SiO_2 layers, and thus the spatial arrangement of nanoparticles in the successive deposited PbTe layers, are not significantly affected by the spatial arrangement of the buried nanoparticles.

Previously proposed theoretical models provided a description of the multilayer structure replication from the dependence of the interlayer correlation length – the distance over which the structure replicates from layer to layer – on the width of the low-order correlation peaks (Salditt *et al.*, 1998; Kegel *et al.*, 1999). These models predict a quadratic $q_{||}$ dependence of the full width at half-maximum (FWHM) $\Delta q_{\rm FWHM}$ of the correlation peaks. Fig. 3 shows $\Delta q_{\rm FWHM}$ *versus* $q_{||}$ plots of the second-order peaks corresponding to PbTe multilayers prepared with the number of laser pulses ($n_{\rm Lp}$) equal to 100, 150 and 200. As can be clearly seen, the quadratic dependence is not observed for any multilayer sample studied. Instead, the $\Delta q_{\rm FWHM}(q_{||})$ curves exhibit two different features: (i) a weak increase of $\Delta q_{\rm FWHM}$ for increasing $q_{||}$ that persists

over a wide range on $q_{||}$, from the smallest $q_{||}$ value up to $q_{||} \simeq 0.4\ \mathrm{nm}^{-1}$ and (ii) a rapid increase of $\Delta q_{\rm FWHM}$ for larger $q_{||}$ values. The weak dependence of $\Delta q_{\rm FWHM}$ with $q_{||}$ for the smaller $q_{||}$ values is probably due to a strong effect on $\Delta q_{\rm FWHM}$ coming from fluctuations in the interlayer distance between nanocrystals. For a particular order this contribution is nearly independent of $q_{||}$ thus leading to a lower limit for $\Delta q_{\rm FWHM}$.

A model to describe the GISAXS of the $PbTe(SiO_2)/SiO_2$ multilayers is presented in §3.1, and in the following sections the GISAXS intensity produced by several $PbTe(SiO_2)/SiO_2$ multilayered samples is analysed separately, in reciprocal space, along directions parallel (in-plane) and normal (out-of-plane) to the external sample surface.

3.1. Modelling of GISAXS intensity from multilayered films

We will here describe the GISAXS intensity produced by a multilayered assembly of spherical nanoparticles embedded in a homogeneous matrix. In this system the nanoparticles are located within a set of parallel two-dimensional layers, exhibiting a spatial lateral correlation, and their sizes are statistically independent of their positions. For this multilayered system the GISAXS intensity can be determined by using the decoupling approximation described by Pedersen (1994). Under this approximation, and accounting also for X-ray refraction effects, the GISAXS intensity is given by

$$I(q_{||}, q_z, \alpha_{\rm i}, \alpha_{\rm f}) \propto (\rho_{\rm p} - \langle\rho\rangle)^2 |T(\alpha_{\rm i})|^2 |T(\alpha_{\rm f})|^2 \times [\langle|F(q, R)|^2\rangle - |\langle F(q, R)\rangle|^2 + |\langle F(q, R)\rangle|^2 S_{\rm tot}(q_{||}, q_z)], \quad (2)$$

where $(\rho_{\rm p} - \langle\rho\rangle)$ is the difference between the electron densities of the nanoparticles $\rho_{\rm p}$ and the multilayer average electron density $\langle\rho\rangle$, $|T(\alpha_{\rm i})|$ and $|T(\alpha_{\rm f})|$ are the effective Fresnel transmission coefficients for an angle of incidence $\alpha_{\rm i}$ and exit angle $\alpha_{\rm f}$, respectively, $\langle|F(q, R)|^2\rangle$ and $|\langle F(q, R)\rangle|^2$ are the *average square* and the *square average*, respectively, of the form factor $F(q, R)$ of a spherical nanoparticle with radius R given by (Glatter & Kratky, 1982)

$$F(q, R) = 4\pi R^3 \frac{\sin(qR) - qR\cos(qR)}{(qR)^3}, \quad (3)$$

$S_{\rm tot}(q_{||}, q_z)$ is the interference function – also named the structure function – that accounts for the spatial correlation between nanoparticles, and $q_{||} = (q_x^2 + q_y^2)^{1/2}$ is the modulus of the photon momentum transfer parallel to the plane containing the particles. Owing to the small volume fraction occupied by PbTe nanocrystals within the total multilayer volume, $\langle\rho\rangle$ is approximately equal to $\rho_{\rm m}$, the electron density of the SiO_2.

The $\langle|F(q, R)|^2\rangle$ and $|\langle F(q, R)\rangle|^2$ functions can be determined from equation (3) and from the nanoparticle radius distribution function $N(R)$ by

$$\langle|F(q, R)|^2\rangle = \frac{\int N(R)|F(q, R)|^2\,{\rm d}R}{\int N(R)\,{\rm d}R} \quad (4)$$

and

$$|\langle F(q, R)\rangle|^2 = \left[\frac{\int N(R)F(q, R)\,{\rm d}R}{\int N(R)\,{\rm d}R}\right]^2, \quad (5)$$

respectively, where $N(R)\,{\rm d}R$ is the number of particles with radius between R and $R + {\rm d}R$.

Concerning the grazing-incidence geometry, if $\alpha_{\rm i}$ and $\alpha_{\rm f}$ are close to the critical angle of total reflection, beside the modulation effect associated with the Fresnel transmission coefficients, $|T(\alpha_{\rm i})|$ and $|T(\alpha_{\rm f})|$ in equation (2), the distribution of the scattered intensity along q_z is also affected by refraction effects. To account for this, the out-of-plane component of the scattering momentum at the detection plane q_z must be replaced by $\tilde{q}_z = 2\pi[\sin_{\rm r}(\alpha_{\rm i}) + \sin_{\rm r}(\alpha_{\rm f})]/\lambda$ (Paniago *et al.*, 1997), where $\sin_{\rm r}(\alpha) = (\sin^2\alpha - 2\delta + 2i\beta)^{1/2}$ and $1 - \delta$ and β are the real and imaginary parts, respectively, of the average index of refraction $n_{\rm R} = 1 - \delta + i\beta$ of the multilayer. In this case, the modulus of the scattering momentum is given by $q = (q_x^2 + q_y^2 + \tilde{q}_z^2)^{1/2}$.

The application of equation (2) to describe the two-dimensional GISAXS intensity pattern is difficult because the interference function $S_{\rm tot}(q_{||}, q_z)$ depends on the spatial distribution of nanocrystals in the layers, which is in general not known. Nevertheless, equation (2) has a simpler behaviour for the GISAXS intensity profile along the q_z axis (*i.e.* for $q_{||} = 0$), normal to the planes of layers. Along the q_z axis the scattered intensity does not depend on any particular configuration or correlation in the lateral (in-plane) positions of nanocrystals and the interference function is only affected by the vertical correlation between layers. If, in addition, we assume that the centres of the nanocrystals in each layer lie in a single plane, *i.e.* if fluctuations in the vertical position (z) of the nanocrystals are negligible, the intensity profile along the z axis, for $q_{||} = 0$, is given by

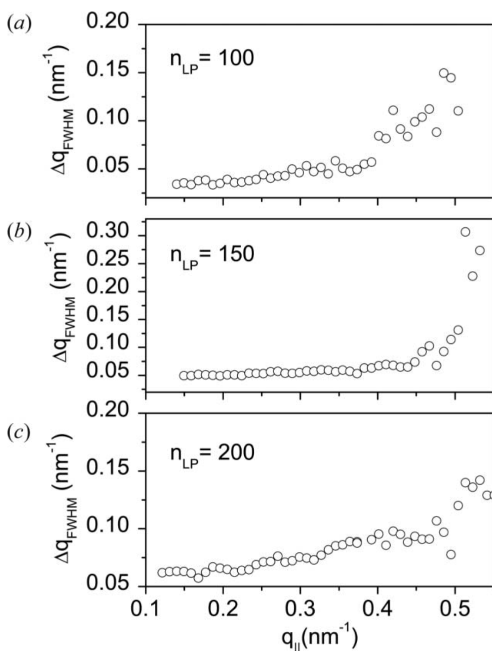

Figure 3
The FWHM $\Delta q_{\rm FWHM}$ of the second-order peak as a function of $q_{||}$ for (*a*) $n_{\rm Lp}$ = 100, (*b*) $n_{\rm Lp}$ = 150 and (*c*) $n_{\rm Lp}$ = 200.

$$I_\perp(0, \tilde{q}_z, \alpha_i, \alpha_f) \propto (\rho_p - \langle\rho\rangle)^2 |T(\alpha_i)|^2 |T(\alpha_f)|^2 [\langle|F(\tilde{q}_z, R)|^2\rangle - |\langle F(\tilde{q}_z, R)\rangle|^2 + |\langle F(\tilde{q}_z, R)\rangle|^2 S_\perp(\tilde{q}_z)]^* V(\tilde{q}_z), \quad (6)$$

where $S_\perp(\tilde{q}_z)$ is the interference function related to the correlation in the vertical position of the layers and $V(\tilde{q}_z)$ is the shape function that accounts for the finite length of the multilayer thickness. The '*' symbol indicates the convolution product.

An approximate equation for $S_\perp(\tilde{q}_z)$ was derived by Hosemann (1951). According to this model, if the fluctuation in the separation of neighbour layers along **z** is approximated by a Gaussian function $p(z) = 1/[\omega_z(2\pi)^{1/2}]\exp[-(z-D)^2/(2\omega_z^2)]$ (ω_z being the standard deviation from the average D value), the interference function is given by (Guinier, 1963)

$$S_\perp(\tilde{q}_z) = \mathrm{Re}\left[\frac{1+P(\tilde{q}_z)}{1-P(\tilde{q}_z)}\right], \quad (7)$$

where

$$P(\tilde{q}_z) = \exp[-\tilde{q}_z^2\omega_z^2/2]\exp[i\tilde{q}_z D]. \quad (8)$$

The $V(\tilde{q}_z)$ function can be calculated from the total thickness of the multilayer L (number of layers times the average distance between the layers D) and is given by (Guinier, 1963)

$$V(\tilde{q}_z) = \frac{\sin^2(\tilde{q}_z L/2)}{(\tilde{q}_z L/2)^2}. \quad (9)$$

In the case that $1/L$ is much smaller than the peak widths, the scattering intensity is only slightly affected by its convolution with $V(\tilde{q}_z)$.

On the other hand, under the assumption that the positions of the nanoparticles located inside each layer are laterally correlated, equation (2) for the in-plane GISAXS intensity becomes

$$I_{||}(q_{||}, q_z, \alpha_i, \alpha_f) \propto (\rho_p - \langle\rho\rangle)^2 |T(\alpha_i)|^2 |T(\alpha_f)|^2 \times [\langle|F(q,R)|^2\rangle - |\langle F(q,R)\rangle|^2 + |\langle F(q,R)\rangle|^2 S_{||}(q_{||})], \quad (10)$$

where $S_{||}(q_{||})$ is the interference function that accounts for the spatial correlation of nanoparticles within each layer. For $q_{||}$ high enough for the interference function to be equal to 1, *i.e.* in the q region where the interference function is not affected by the lateral spatial correlation, equation (10) becomes

$$I_{||}(q_{||}, q_z, \alpha_i, \alpha_f) \propto (\rho_p - \langle\rho\rangle)^2 |T(\alpha_i)|^2 |T(\alpha_f)|^2 \langle|F(q,R)|^2\rangle. \quad (11)$$

In practice, equation (11) can only be applied to real systems for the determination of the size distribution of the nanoparticles in the case in which the structure function is equal to 1 in most of the $q_{||}$ range, *i.e.* for systems that exhibit a low or moderate spatial correlation.

In short, even though the system studied here is *a priori* described by a rather complex interference function that involves correlation within each layer and also between them, we have here described how to independently access the size distribution of the spherical nanoparticles, by analysing in-plane GISAXS profiles $I_{||}$ [equation (11)], and the structure parameters related to the correlation along the direction normal to the layers, by analysing the out-of-plane ($I_\perp$) GISAXS intensity for $q_{||} = 0$ [equations (6) to (9)].

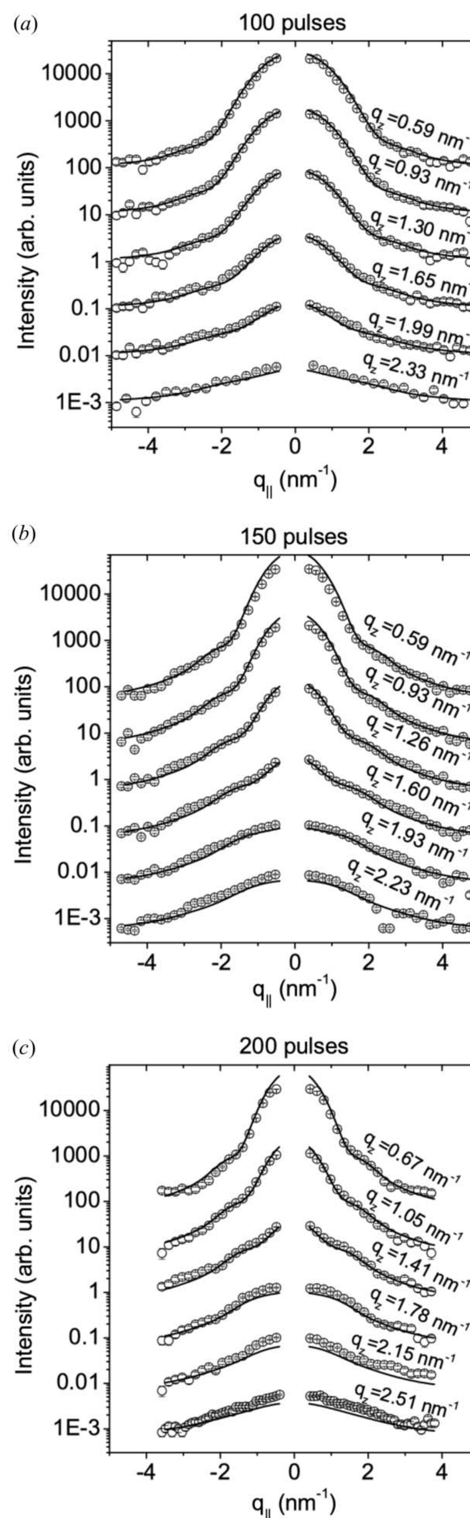

Figure 4
In-plane GISAXS profiles corresponding to $PbTe(SiO_2)/SiO_2$ multilayers on an Si(111) substrate for different amounts of deposited PbTe, n_{Lp}: (*a*) 100, (*b*) 150 and (*c*) 200. The solid lines are the best fits to the experimental data using equation (11).

3.2. Experimental in-plane GISAXS profiles and model fitting

Fig. 4 displays the X-ray scattering profiles along the $q_{\|}$ axis for different q_z values, corresponding to multilayered samples prepared with three different PbTe contents ($n_{\rm Lp}$ = 100, 150 and 200). The intensity profiles along the y axis were arbitrarily chosen at q_z values located between scattering intensity maxima. In the small $|q_{\|}|$ region, the intensity is affected by the interference function accounting for the correlation between the nanocrystals' positions. This generates negative deviations in the SAXS intensity over the small $|q_{\|}|$ region, as compared to the intensity associated with a dilute set of nanocrystals. Conversely, for profiles along the y axis, for q_z values corresponding to the maxima of the $S_{\rm tot}(q_{\|}, q_z)$ function (not shown), the deviation in the SAXS intensity at small $|q_{\|}|$ is positive.

Nevertheless, for $|q_{\|}|$ values larger than about 0.7 nm^{-1} the $S_{\|}$ function does not significantly differ from unity and thus the in-plane scattering intensity profiles are only slightly affected by it. Thus, for $|q_{\|}| > 0.7$ nm^{-1}, the in-plane total GISAXS intensity is given by equation (11).

A Gaussian function $N_{\rm G} = 1/[\sigma_{\rm R}(2\pi)^{1/2}]\exp[-(R - \langle R\rangle)^2/(2\sigma_{\rm R}^2)]$ was selected in order to tentatively describe the radius distribution function $N(R)$ of the PbTe nanocrystals, $\langle R\rangle$ and $\sigma_{\rm R}$ being the average radius and the radius dispersion of nanocrystals, respectively.

The modelled curves corresponding to the best fit to experimental data using equation (11) for all analysed samples ($n_{\rm Lp}$ = 100, 150 and 200) are displayed in Fig. 4 (solid lines).

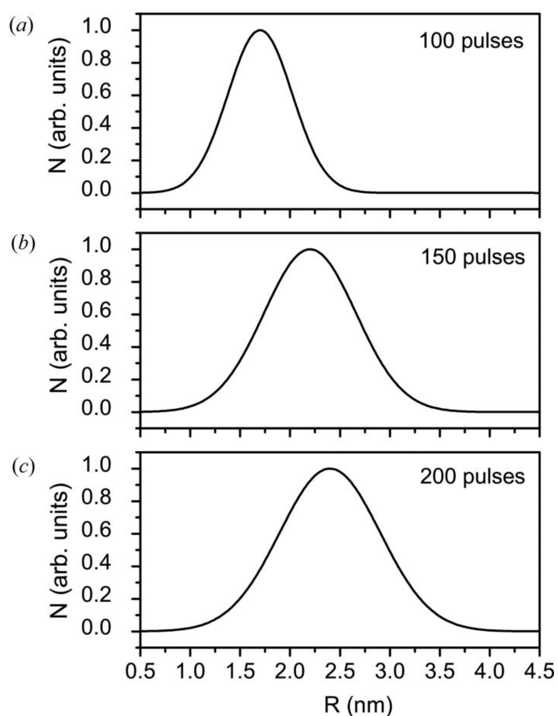

Figure 5
Gaussian radius distribution functions in arbitrary units $N_{\rm G}(R)$ derived from modelled scattering intensity corresponding to different numbers of laser pulses for PbTe deposition. The maxima of the $N_{\rm G}(R)$ curves were normalized to unity.

Table 1
Average PbTe nanocrystal radius $\langle R\rangle$, relative radius dispersion $\sigma_{\rm R}/\langle R\rangle$, and ratio between the number of laser pulses and nanocrystal average volume $n_{\rm Lp}/\langle V\rangle$.

$n_{\rm Lp}$	$\langle R\rangle$ (nm)	$\sigma_{\rm R}/\langle R\rangle$	$n_{\rm Lp}/\langle V\rangle$ (relative units)
100	1.65 (5)	0.19 (2)	18.4 (6)
150	2.20 (5)	0.21 (2)	12.4 (4)
200	2.40 (5)	0.21 (2)	12.8 (4)

The deviation of the scattering intensity profiles from the best-fitting curves using equation (11) in the portion of the scattering curves over the small $|q_{\|}|$ range is due to the effect of the structure function discussed above. This effect is more apparent for GISAXS profiles corresponding to multilayer samples prepared with 150 and 200 laser pulses. Nevertheless, the good agreement between the experimental and theoretical curves for high momentum transfer, in which $S_{\rm tot}$ is essentially equal to unity and the scattering curves only depend on the average square of the nanoparticle form factor, ensures the satisfactory accuracy of the $\langle R\rangle$ and $\sigma_{\rm R}/\langle R\rangle$ values determined here.

The Gaussian radius distribution functions, $N_{\rm G}(R)$, derived from the modelled scattering intensity curves corresponding to different PbTe contents are plotted in Fig. 5. Our experimental results indicate a progressive increase in the nanocrystal average radius and a slight increase in the radius dispersion [standard deviation of the $N(R)$ curves] for increasing PbTe content, evidenced by a shift of the maximum of the distribution toward higher R and by the increasing FWHM of the $N_{\rm G}(R)$ curves, respectively. From the $N_{\rm G}(R)$ function obtained using the fitting procedure described above applied to the whole set of scattering profiles at different q_z values, the nanocrystal average radius $\langle R\rangle$ and the relative radius dispersion $\sigma_{\rm R}/\langle R\rangle$ were determined. The results are reported in Table 1.

3.3. Experimental out-of-plane GISAXS profiles and model fitting

Fig. 6 displays the out-of-plane GISAXS intensity profiles ($I_\perp$ *versus* q_z) at $q_{\|} = 0.16$ nm^{-1} for multilayers prepared with different PbTe contents, *i.e.* different number of applied laser pulses. These curves were measured in this case at a longer sample-to-detector distance in order to have access to smaller photon momentum transfers. The incidence angle was adjusted to $\alpha_{\rm i} = 0.5°$. For this incidence angle the penetration depth Λ estimated from the nominal composition of the sample and from the experimental conditions reported above is equal to 793 and 505 nm for multilayers prepared with 100 and 200 laser pulses, respectively. This penetration depth is much larger than the total multilayer thickness, equal to $20D$, so that the scattering patterns probed the structure of the whole multilayered films. At $q_z \simeq 0.5$ nm^{-1} the tail of the first-order correlation peak modulated by the Fresnel transmission coefficient function $|T(\alpha_{\rm f})|$ can be observed. The intensity of the higher-order Bragg peaks decreases for increasing q_z. For the GISAXS profile at $q_z = 0.87$ nm^{-1} corresponding to a

multilayer prepared by applying a particular number of laser pulses, $n_{\rm Lp}$ = 100, the tail of the reflected beam is also observed. For all samples studied, the amplitudes of the correlation peaks of the scattering patterns decrease for increasing q_z values. We have also noticed an increase in the width of the peaks for increasing $n_{\rm Lp}$ values. This effect of peak broadening suggests an increase in disorder in the multilayer spacing D for increasing numbers of laser pulses for PbTe deposition.

In order to characterize the structure and the structural disorder related to the set of regularly spaced PbTe nanocrystal layers, the GISAXS profile along the direction normal to the multilayer surface (q_z axis) was analysed by applying the theory described in §3.1.

The solid lines corresponding to the best fit of the GISAXS curves modelled by equations (6)–(9) to the experimental profiles, along the q_z (out-of-plane) axis, are displayed in Fig. 6. In the analysis we assume that these equations that hold for $q_{\|} = 0$ are still a good approximation for the intensity profiles at the small in-plane scattering momentum $q_{\|} = 0.16\ {\rm nm}^{-1}$. To partially account for the fact that the $I_{\perp}$ *versus* q_z intensity profiles are taken slightly off the q_z axis, $F(\tilde{q}_z, R)$ was replaced by $F(q, R)$ in equation (6). The results of the fittings to the experimental profiles indicate that the average radius $\langle R \rangle$ and the relative radius dispersion $\sigma_{\rm R}/\langle R \rangle$ are equivalent to those previously determined from the best fit to in-plane scattering profiles (Table 1). In spite of their small effect on the shape of GISAXS curves the convolutions by the overall multilayer shape factor $V(\tilde{q}_z)$ and X-ray beam resolution were accounted for in the fitting procedure.

A good fit to experimental data, showing the main features of the out-of-plane intensity profiles at the small q_z region, was obtained for samples with $n_{\rm Lp}$ = 100 and 200. Nevertheless a clear deviation was observed over the same q_z range for samples with $n_{\rm Lp}$ = 150. We have attributed this deviation to the approximation used for the effective transmission function, which neglects internal X-ray multiple reflection–refractions (Holý & Ohlídal, 1993). The procedure applied here, in which several orders of scattering reflections were fitted simultaneously, allowed us to determine the average period of multilayers D as well as the disorder parameter ω_z that characterizes the fluctuations in the average period. The values of D and ω_z obtained from the best fit to experimental data using equations (6)–(9) are reported in Table 2.

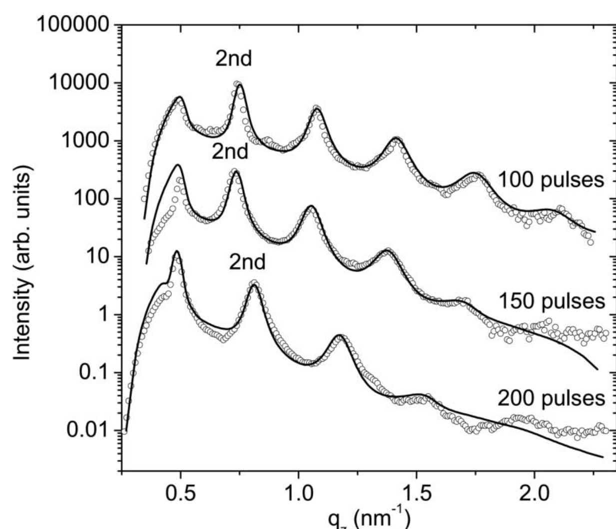

Figure 6
Out-of-plane experimental GISAXS profiles ($I_{\perp}$ *versus* q_z) at $q_{\|}$ = 0.16 nm^{-1} corresponding to $PbTe(SiO_2)/SiO_2$ multilayers, for the indicated numbers of laser pulses (symbols). The second-order correlation peak is indicated. The solid lines are the best-fitted curves using equations (6)–(9) to the experimental GISAXS profiles.

Table 2
Average period of $PbTe(SiO_2)/SiO_2$ multilayers D, standard deviation of the interlayer distances ω_z, and relative dispersion in interlayer distances ω_z/D, for different numbers of laser pulses applied to the deposition of each PbTe layer $n_{\rm Lp}$.

$n_{\rm Lp}$	D (nm)	ω_z (nm)	ω_z/D (%)
100	18.3 (1)	0.95 (5)	5.2
150	18.8 (1)	1.07 (5)	5.7
200	16.8 (2)	1.02 (5)	6.1

4. Discussion

4.1. In-plane small-angle X-ray scattering

The average PbTe nanocrystal radius $\langle R \rangle$ determined by the best-fitting procedure is reported in Table 1 as a function of the number of laser pulses, $n_{\rm Lp}$. This result indicates an increase in nanocrystal radius for an increasing number of laser pulses, or PbTe content. This increase suggests that increasing amounts of deposited PbTe per layer promote the formation of progressively larger PbTe nanocrystals.

The results reported in Table 1 indicate a weak variation in relative radius dispersion $\sigma_{\rm R}/\langle R \rangle$, ranging from 0.19 to 0.21 for $n_{\rm Lp}$ equal to 100 and 200, respectively, thus indicating that $\sigma_{\rm R}/\langle R \rangle$ is only slightly affected by the number of pulses used in PbTe deposition. For the multilayer prepared with $n_{\rm Lp}$ = 150, $\sigma_{\rm R}/\langle R \rangle$ is the same as the ratio corresponding to the sample with $n_{\rm Lp}$ = 200 ($\sigma_{\rm R}/\langle R \rangle$ = 0.21).

The results reported in Table 1 also indicate that, when the number of laser pulses (or PbTe content) is increased by a factor 2 ($n_{\rm Lp}$ increased from 100 to 200), the average nanocrystal volume increases by a higher factor, *i.e.* ~2.8. This suggests that the effect of volume increase for an increasing number of laser pulses is accompanied by a parallel decrease in the specific number of nanocrystals. By quantitatively assuming that the total volume occupied by PbTe nanocrystals $V_{\rm tot}$ is proportional to the number of laser pulses $n_{\rm Lp}$ used in the deposition process, we have

$$V_{\rm tot} \propto n_{\rm Lp}. \qquad (12)$$

On the other hand, we can write $V_{\rm tot} = n\langle V \rangle$ where $\langle V \rangle$ is the average volume and n is the specific number of PbTe nanocrystals, so that the specific number of nanocrystals can be written as

$$n \propto n_{\rm Lp}/\langle V \rangle. \qquad (13)$$

The average volume of PbTe nanocrystals $\langle V \rangle$ can be calculated from the radius distribution function $N_G(R)$ derived from our analysis of the SAXS intensity by

$$\langle V \rangle = \frac{4\pi}{3} \frac{\int_0^\infty N_G(R) R^3 \, dR}{\int_0^\infty N_G(R) \, dR}. \quad (14)$$

The $n_{Lp}/\langle V \rangle$ ratios, or number density of nanocrystals n in relative scale, determined by applying equation (13) for different numbers of laser pulses n_{Lp} are reported in Table 1. These results indicate that the number density of nanocrystals is the highest in the multilayered sample prepared with n_{Lp} equal to 100. The number density is 50% lower for the sample prepared with 150 laser pulses. For samples prepared with 150 and 200 laser pulses no significant variation in the number density of nanocrystals is apparent.

The decrease in the number density of nanocrystals for increasing amounts of deposited Pb and Te atoms could be the consequence of the coalescence of very closely located nanoclusters (Serna *et al.*, 1999). During the deposition process and as a consequence of their progressive growth, nanoclusters located at a distance smaller than the sum of the increment in their radius may coalesce, thus giving rise to a single and larger cluster.

An alternative explanation for the behaviour mentioned above – the increase in average radius of PbTe nanocrystals, decrease in their number density and nearly constant relative radius dispersion ($\sim$0.2) – may be the action of a process of nanocrystal coarsening. During the deposition stage of each single pulse, an increase in temperature promoted by the ablated vapour may lead to the dissolution of the smaller, less stable, clusters into mobile atoms attaching to larger, more stable, clusters. This process is analogous to the coarsening mechanism yielding a growth of the average cluster radius at advanced stages of thermal annealing in supersaturated solid solutions at high temperatures (Lifshitz & Slyozov, 1961; Wagner, 1961). The driving force for coarsening is related to the reduction of interface energy and thus of the total nanoparticle surface. During the coarsening stage, large clusters grow at the expense of the small ones while the relative size dispersion is kept constant and approximately equal to 0.22. In the case of the PbTe multilayers investigated here, the activation energy necessary to the diffusion of the Pb and Te species through the vitreous SiO_2 matrix could be provided by the high-temperature-ablated vapour. In fact, evidence of the rather high temperature reached locally during the deposition process is the spherical shape of the nanoparticles themselves. The fact that the nanoparticles are nearly spherical instead of being clusters with planar or other anisotropic shapes (Metev & Meteva, 1989) is consistent with the existence of precursor liquid droplets whose spherical shape is the expected consequence of the action of isotropic hydrostatic pressure. Following the vapour deposition stage, the temperature decreases and, thus, the nanoparticles crystallize, keeping approximately the shape of the precursor liquid droplets.

A more detailed description of the mechanism of growth of PbTe nanoparticles requires additional studies including TEM experiments and direct measurements of the substrate temperature combined with XRD measurements to monitor the nanoparticle phase (crystalline or liquid) during the deposition process.

4.2. Out-of-plane small-angle X-ray scattering

The results derived from the out-of-plane scattering profiles reported in Table 2 indicate that the multilayer period D is nearly equivalent for samples prepared by applying 100 and 150 laser pulses ($D \simeq 18$ nm) and slightly smaller ($D \simeq 16$ nm) for the sample prepared by applying 200 laser pulses. Since the deposition parameters of SiO_2 layers were kept the same, the observed dependence of the period D on the number of laser pulses (Table 2) is not *a priori* expected. As a matter of fact, increasing amounts of deposited Pb and Te atoms promoted by an increasing number of laser pulses are expected to yield multilayers with a progressively higher period. In order to clarify this issue additional GISAXS experiments on PbTe/SiO_2 multilayers over a wide range of PbTe concentrations are being planned. On the other hand, the rather small values of the ω_z/D ratio (5.2, 5.7 and 6.1% for n_{Lp} equal to 100, 150 and 200, respectively) indicate that the deposition conditions do not change considerably during the preparation process of each single PbTe(SiO_2)/SiO_2 multilayer.

5. Conclusions

The structure of PbTe(SiO_2)/SiO_2 multilayers deposited on an Si(111) substrate was studied by the grazing-incidence small-angle X-ray scattering technique using synchrotron radiation. The experimental scattering patterns are consistent with the results of previous TEM experiments showing that the PbTe layers are formed by a set of nearly spherical PbTe nanocrystals.

The analysis of the in-plane GISAXS results allowed us to determine the average radius, the radius dispersion and the number density (in relative units) of PbTe nanocrystals as functions of the PbTe content or number of laser pulses used in the deposition of each PbTe layer. Our results indicate a progressive increase in the PbTe nanocrystal average radius for increasing PbTe content. The increase in the average radius is accompanied by a diminution in the number density of nanocrystals, thus suggesting the coalescence and/or coarsening of the PbTe nanoparticles for increasing amounts of deposited PbTe. The ratio between the standard deviation of the radius distribution function and the nanoparticle average radius exhibits a small variation within the 0.19–0.21 range.

Finally, by applying the paracrystal model derived by Hosemann (1951) to fit the experimental GISAXS profiles along the direction normal to the sample surface (out-of-plane scattering), the average interlayer distance and the parameter that characterizes the fluctuations in interlayer distances were determined. The low values of the relative dispersion in interlayer distances (5.2–6.1%) over a large surface area

(3 × 20 mm) indicate a rather good quality of the PbTe(SiO_2)/SiO_2 multilayers prepared by pulsed laser deposition.

This work was supported by the Brazilian Synchrotron Light Laboratory (LNLS) and the Brazilian funding agencies PRONEX, CNPq and FAPESP.

References

Acapito, F. d', Maurizio, C., Gonella, F., Cattaruzza, E., Mattei, G., Mondelli, C., Longo, A. & Martorana, A. (2004). *J. Synchrotron Rad.* **11**, 272–277.
Babonneau, D., Petroff, F., Maurice, J.-L., Fettar, F., Vaurès, A. & Naudon, A. (2000). *Appl. Phys. Lett.* **76**, 2892–2894.
Buljan, M., Salamon, K., Dubcek, P., Bernstorff, S., Desnica-Frankovic, I. D., Milat, O. & Desnica, U. V. (2003). *Vacuum*, **71**, 65–70.
Cohen, J. B. & Chung, Y. W. (1991). *Surf. Sci.* **248**, 215–224.
Craievich, A., Kellermann, G., Barbosa, L. C. & Alves, O. L. (2002). *Phys. Rev. Lett.* **89**, 235503.
Desnica, U. V., Buljan, M., Desnica-Frankovic, I. D., Dubcek, P., Bernstor, S., Ivanda, M. & Zorc, H. (2004). *Nucl. Instrum. Methods Phys. Res. Sect. B*, **216**, 407–413.
Efros, Al. L. & Efros, A. L. (1982). *Sov. Phys. Semicond.* **16**, 772–775.
Glatter, O. & Kratky, O. (1982). *Small Angle X-ray Scattering*. London: Academic Press.
Gleiter, H. (1989). *Prog. Mater. Sci.* **33**, 223–315.
Guinier, A. (1963). *X-ray Diffraction in Crystals, Imperfect Crystals and Amorphous Bodies*. New York: Dover Publications.
Holý, V., Kubena, J. & Ohlídal, I. (1993). *Phys. Rev. B*, **47**, 15896–15903.
Holý, V., Pietsch, U. & Baumbach, T. (1999). *High-Resolution X-ray Scattering from Thin Films and Multilayers*, Springer Tracts in Modern Physics No. 149. Berlin: Springer Verlag.
Hosemann, R. (1951). *Acta Cryst.* **4**, 520–530.
Kegel, I., Metzger, T. H., Peisl, J., Stang, J., Bauer, G. & Smilgies, D. (1999). *Phys. Rev. B*, **60**, 2516–2521.
Lifshitz, I. M. & Slyozov, V. V. (1961). *Phys. Chem. Solids*, **19**, 35–50.
Metev, S. & Meteva, K. (1989). *Appl. Surf. Sci.* **43**, 402–408.
Paniago, R., Forrest, R., Chow, P. C., Moss, S. C., Parkin, S. S. P. & Cookson, D. (1997). *Phys. Rev. B*, **56**, 13442–13454.
Pedersen, J. S. (1994). *J. Appl. Cryst.* **27**, 595–608.
Rauscher, M., Paniago, R., Metzger, H., Kovats, Z., Domke, J. & Peisl, J. (1999). *J. Appl. Phys.* **86**, 6763–6769.
Reynoso, V. C. S., de Paula, A. M., Cuevas, R. F., Medeiros Neto, J. A., Alves, O. L., Cesar, C. L. & Barbosa, L. C. (1995). *Electron. Lett.* **31**, 1013–1015.
Rodriguez, E., Jimenez, E., Chillcce, E. F., Cesar, C. L. & Barbosa, L. C. (2006). *Proc. SPIE*, **6321**, 63210L.
Rodriguez, E., Jimenez, E., Padilha, L. A., Neves, A. A. R., Jacob, G. J., Cesar, C. L. & Barbosa, L. C. (2005). *Appl. Phys. Lett.* **86**, 113117.
Salditt, T., Lott, D., Metzger, T. H., Peisl, J., Vignaud, G., Høghøj, P., Schärpf, O., Hinze, P. & Lauer, R. (1998). *Phys. Rev. B*, **54**, 5860–5872.
Salditt, T., Metzger, T. H. & Peisl, J. (1994). *Phys. Rev. Lett.* **73**, 2228–2231.
Serna, R., Afonso, C. N., Ballesteros, J. M., Naudon, A., Babonneau, D. & Petford-Long, A. K. (1999). *Appl. Surf. Sci.* **138–139**, 1–5.
Tolan, M. (1999). *X-ray Scattering from Soft-Matter Thin Films: Material Science and Basic Research.* Berlin: Springer.
Tsunetomo, K., Ohtsuka, S., Koyama, T., Tanaka, S., Sasaki, F. & Kobayashi, S. (1995). *Mol. Cryst. Liq. Cryst. Sci. Technol. Sect. B*, **13**, 109–126.
Wagner, C. (1961). *Z. Elektrochem.* **65**, 581–594.